Multilayer electronic arrays
on balloon catheters

Catheter-integrated soft multilayer electronic arrays for multiplexed sensing and actuation during cardiac surgery

Mengdi Han [1,20], Lin Chen [2,3,20], Kedar Aras [4,20], Cunman Liang [5], Xuexian Chen [6], Hangbo Zhao [1,7], Kan Li [2,8,9,10], Ndeye Rokhaya Faye [4], Bohan Sun [1,11], Jae-Hwan Kim [12,13], Wubin Bai [1,9], Quansan Yang [8], Yuhang Ma [1,14], Wei Lu [1], Enming Song [1], Janice Mihyun Baek [15], Yujin Lee [15], Clifford Liu [1], Jeffrey B. Model [1], Guanjun Yang [3], Roozbeh Ghaffari [1,16], Yonggang Huang [1,2,8,9 ✉], Igor R. Efimov [4 ✉] and John A. Rogers [1,8,9,12,16,17,18,19 ✉]

The rigidity and relatively primitive modes of operation of catheters equipped with sensing or actuation elements impede their conformal contact with soft-tissue surfaces, limit the scope of their uses, lengthen surgical times and increase the need for advanced surgical skills. Here, we report materials, device designs and fabrication approaches for integrating advanced electronic functionality with catheters for minimally invasive forms of cardiac surgery. By using multiphysics modelling, plastic heart models and Langendorff animal and human hearts, we show that soft electronic arrays in multilayer configurations on endocardial balloon catheters can establish conformal contact with curved tissue surfaces, support high-density spatiotemporal mapping of temperature, pressure and electrophysiological parameters and allow for programmable electrical stimulation, radiofrequency ablation and irreversible electroporation. Integrating multimodal and multiplexing capabilities into minimally invasive surgical instruments may improve surgical performance and patient outcomes.

Minimally invasive surgeries involve the insertion of advanced diagnostic and therapeutic tools through small percutaneous incisions for treatment of cardiovascular diseases, cancers and other health conditions, with fast recovery times and low risks compared with those of conventional procedures[1,2]. Catheters represent one of the most compelling devices for such purposes due to their capabilities in deploying medical devices (for example, intravascular stents or heart-valve prostheses), capturing information during surgical procedures (for example, force, temperature or electrograms) and/or delivering forces, electromagnetic energy, thermal stimuli and/or biomaterials (for example, drugs, cells or nanoparticles) to targeted sites on or within soft tissues[3,4]. Although these catheter-based approaches have widespread uses in modern medicine, they suffer from (1) mechanical rigidity or insufficient compliance, leading to non-ideal interfaces with soft tissues and low coupling efficiency[5], (2) limited spatial densities and array configurations of sensing or actuating elements, leading to the need for asynchronous 'roving-probe' procedures and guided

placement for effective diagnosis and therapy[6], and (3) narrow functional options, leading to requirements for insertion and navigation of multiple catheters in the context of a single surgery[7].

Instrumenting catheters with advanced electronic components, sensors and actuators may establish a means to overcome these shortcomings[8–12]. Emerging strategies in soft electronics that leverage materials and fabrication capabilities adapted from the semiconductor industry have potential to provide immediate opportunities in this context[13–15]. An essential goal is in the construction of networks of integrated elements that support multimodal diagnostic and therapeutic functions in addressable, interconnected array configurations. This paper describes progress in this area, with an emphasis on two- and three-dimensional (2D and 3D) device architectures, layered configurations and advanced modalities. The specific advances over previous systems[8,16–19] include (1) instrumented sensors and actuators in multiplexed array formats, with spatial densities designed to probe the complex nature of tissues, specifically the heart (for example, the more than 10^9 cardiomyocytes in

[1]Querrey Simpson Institute for Bioelectronics, Northwestern University, Evanston, IL, USA. [2]Departments of Civil and Environmental Engineering, Northwestern University, Evanston, IL, USA. [3]State Key Laboratory for Mechanical Behavior of Materials, School of Materials Science and Engineering, Xi'an Jiaotong University, Xi'an, China. [4]Department of Biomedical Engineering, The George Washington University, Washington, DC, USA. [5]Key Laboratory of Mechanism Theory and Equipment Design of Ministry of Education, School of Mechanical Engineering, Tianjin University, Tianjin, China. [6]Academy for Advanced Interdisciplinary Studies, Peking University, Beijing, China. [7]Department of Aerospace and Mechanical Engineering, University of Southern California, Los Angeles, CA, USA. [8]Department of Mechanical Engineering, Northwestern University, Evanston, IL, USA. [9]Department of Materials Science and Engineering, Northwestern University, Evanston, IL, USA. [10]Department of Engineering, University of Cambridge, Cambridge, UK. [11]Department of Mechanical Engineering, Johns Hopkins University, Baltimore, MD, USA. [12]Frederick Seitz Materials Research Laboratory, University of Illinois at Urbana–Champaign Urbana, Champaign, IL, USA. [13]Department of Electrical and Computer Engineering, University of Illinois at Urbana–Champaign Urbana, Champaign, IL, USA. [14]School of Chemical Engineering and Technology, Tianjin University, Tianjin, China. [15]Department of Chemistry, University of Illinois at Urbana–Champaign Urbana, Champaign, IL, USA. [16]Department of Biomedical Engineering, Northwestern University, Evanston, IL, USA. [17]Department of Surgery, Northwestern University Feinberg School of Medicine, Chicago, IL, USA. [18]Department of Chemistry, Northwestern University, Evanston, IL, USA. [19]Department of Electrical Engineering and Computer Science, Northwestern University, Evanston, IL, USA. [20]These authors contributed equally: Mengdi Han, Lin Chen, Kedar Aras. ✉e-mail: y-huang@northwestern.edu; efimov@gwu.edu; jrogers@northwestern.edu

the human heart[20]); (2) multilayer architectures with combined diagnostic and therapeutic functions, including the latest cardiac procedures that rely on electroporation; and (3) capabilities in real-time feedback control, enabled by simultaneous, multimodal operation of sensors and actuators. The specific systems reported here allow conformal contacts with tissues for simultaneous, multimodal mapping of temperature, pressure and electrophysiological parameters, with options in programmable actuation of thermal inputs and electrical stimulation, radiofrequency ablation (RFA) and/or irreversible electroporation (IRE) at soft-tissue surfaces. Studies on Langendorff rabbit and human hearts demonstrate the multifunctionality and high measurement fidelity of the systems, and computational models highlight the underlying mechanisms.

Results

Multimodal, multiplexed soft electronics. Figure 1a presents a schematic illustration of the device platform. Multifunctional collections of sensors, actuators and associated electronics mount on elastic surfaces in multilayer designs in which each layer serves a distinct function. Stretchable interconnects made from gold (Au) (100 to 300 nm in thickness, 15 to 50 μm in width) sandwiched in polyimide (PI) (1 to 3.3 μm in thickness, 21 to 100 μm in width) create multiplexed arrays covering areas of ~1 cm × 1 cm. The network demonstrated here includes electrodes (8 × 8) for electrophysiological recording and electrical stimulation (that is, for RFA and IRE), temperature sensors (8 × 8) for precision thermography and pressure sensors (8 × 8) for measuring the forces associated with soft-tissue contact, corresponding collectively to capabilities in multifunctional spatiotemporal mapping. Fabrication exploits microfabrication techniques adapted from those used in the semiconductor industry to build multiple layers of sensing elements, actuators and ultrathin polymers (1 to 3.3 μm in thickness) using silicon wafers as temporary substrates and transfer printing methods to deliver these layers to soft, elastomeric substrates. Strategies in compressive buckling[21] transform parts of these structures into 3D configurations to enable their targeted performance. These methods support high spatial densities (~160 cm−2) of sensors and actuators, while leveraging fast switching and multiplexing capabilities across rows and columns of elements.

Supplementary Note 1 and Supplementary Figs. 1–3 illustrate the fabrication processes for each layer. The soft and stretchable mechanics of these systems facilitate mounting on a variety of curvilinear surfaces. Minimally invasive tools, such as balloon catheter-based systems, represent a compelling opportunity for this integration, due primarily to an unmet need for dense, multifunctional capabilities in the context of diagnostic and therapeutic surgical procedures, specifically in endocardial electrophysiology and ablation. Figure 1b shows a representative balloon catheter instrumented with an electrode array (8 × 8) deployed inside the left atrium of a transparent heart model. Thin copper (Cu) traces (18 μm in thickness, 60 μm in width, 60 μm in spacing) connect the array at the distal end of the balloon catheter to wired connections that route through the catheter extrusion (insets in Fig. 1b and Supplementary Fig. 4).

Precise multiparametric measurements, effective treatments and optimal mechanics (that is, elastic response to compression during deflation and stretching during inflation of the balloon) require careful axial orientation of each layer of sensors and actuators. In this multilayered configuration, the electrode arrays reside on the topmost surface to enable direct contact with biological tissues. Temperature sensors lie subjacent to the electrodes, separated by a thin insulating layer of PI (~6 μm in thickness), to allow tracking of changes in temperature associated with ablation or other procedures. The layer with pressure sensors is located at the bottom, for measurements of the local transverse forces at the interface between the electrodes and the contacting soft tissues (Supplementary Fig. 5).

The vertical stack of arrays of electrodes, temperature sensors and pressure sensors joins the sensing units together as the nodes of the multilayer mesh (positioning and overlay accuracy better than 100 μm across the whole array), but leaves the stretchable interconnects untethered to the elastomeric substrate to enable out-of-plane deformations for enhanced stretchability (>30% of biaxial stretch). Detailed fabrication procedures are presented in Supplementary Note 1 and Supplementary Figs. 6 and 7. Figure 1c,d shows images of the multilayer electronic system with arrays of sensing elements (~0.8 × 0.8 mm in lateral dimension for each pixel) and interconnects embedded in each layer.

The electrode array consists of exposed Au pads (500 μm × 500 μm in lateral dimension, 300 nm in thickness) interconnected by serpentine traces and sandwiched between two layers of PI (3.3 μm in thickness each). These traces adopt optimal geometric designs (Au: 15 μm in width; PI: 21 μm in width) to accommodate biaxial stretching of 30% without inducing fractures in the constituent materials (Fig. 1e and Supplementary Figs. 8 and 9). A multiplexed data-acquisition system includes an application-specific integrated circuit (ASIC) chip (RHD2164, Intan Technologies) to amplify, digitize and multiplex the signals, thereby reducing the total number of wires that connect to the testing instrument from 64 to 8 (Supplementary Fig. 10). Using the ASIC chip eliminates the requirement for flexible transistors at each unit cell and enables the system to leverage state-of-the-art microelectronic elements (Supplementary Table 1). In vitro measurements on the electrode array indicate an ability to reach 100% yields, with high levels of uniformity (impedances with a mean of 9,547 Ω and s.d. of 192.5 Ω under Gaussian fitting) and stretchability (toleration to biaxial tensile strains of 30%) and stable impedances under various conditions (for example, after stacking with more layers of electronics, under 30% biaxial stretching, and after 10,000 cycles of 20% uniaxial stretching, Supplementary Figs. 11–13).

Similar to the electrode array design, the temperature sensor array exploits thin metal traces of Au (100 nm in thickness, 4 μm in width), but configured as resistive elements, each electrically interfaced to two connection lines. This feature enables column and row selection multiplexing using signals delivered through these lines[22]. The lines for row selection reside in the layer with the temperature sensor, whereas those for column selection lie above, separated by a layer of PI (1 μm in thickness) and connected to one side of the sensors through a via hole (~24 × 30 μm in area) (Fig. 1f and Supplementary Figs. 14 and 15). An 8 × 8 array of temperature sensors in this configuration yields sixteen wires, eight for row selection and eight for column selection. A customized circuit mounted outside of the array enables multiplexing of the signals and eliminates crosstalk with proper grounding (Supplementary Figs. 16–19 and Supplementary Table 1). A 5 kHz clock signal allows each individual sensor to record temperatures at a sampling rate of ~40 Hz. Averaged outputs from sixty-four temperature sensors yield a precision (one s.d.) ranging from ~20 to ~50 mK (n = 61) (Supplementary Fig. 20). Synchronized temperature recordings from an infrared camera and the sensor array under irradiation by ultraviolet (UV) laser to create a distribution of heating by optical absorption verify the accuracy of the system (Supplementary Fig. 19 and Supplementary Video 1). Measurements captured without grounding suffer from leakage currents, leading to poor spatiotemporal temperature-mapping results (Supplementary Figs. 21 and 22). In vitro characterization results (Supplementary Figs. 23 and 24) illustrate uniform sensitivity (temperature coefficients of resistances (TCRs), with a mean of 0.17% and s.d. of 0.0007% under Gaussian fitting), linear responses from 30 to 80 °C ($R^2 > 0.9999$ in linear regression before and after stacking with other layers of electronics), as well as mechanical robustness (stable resistance under biaxial strains of 30% and 10,000 cycles of 20% uniaxial stretching). The array of temperature sensors can also be exploited for spatial mapping of tissue thermal conductivity
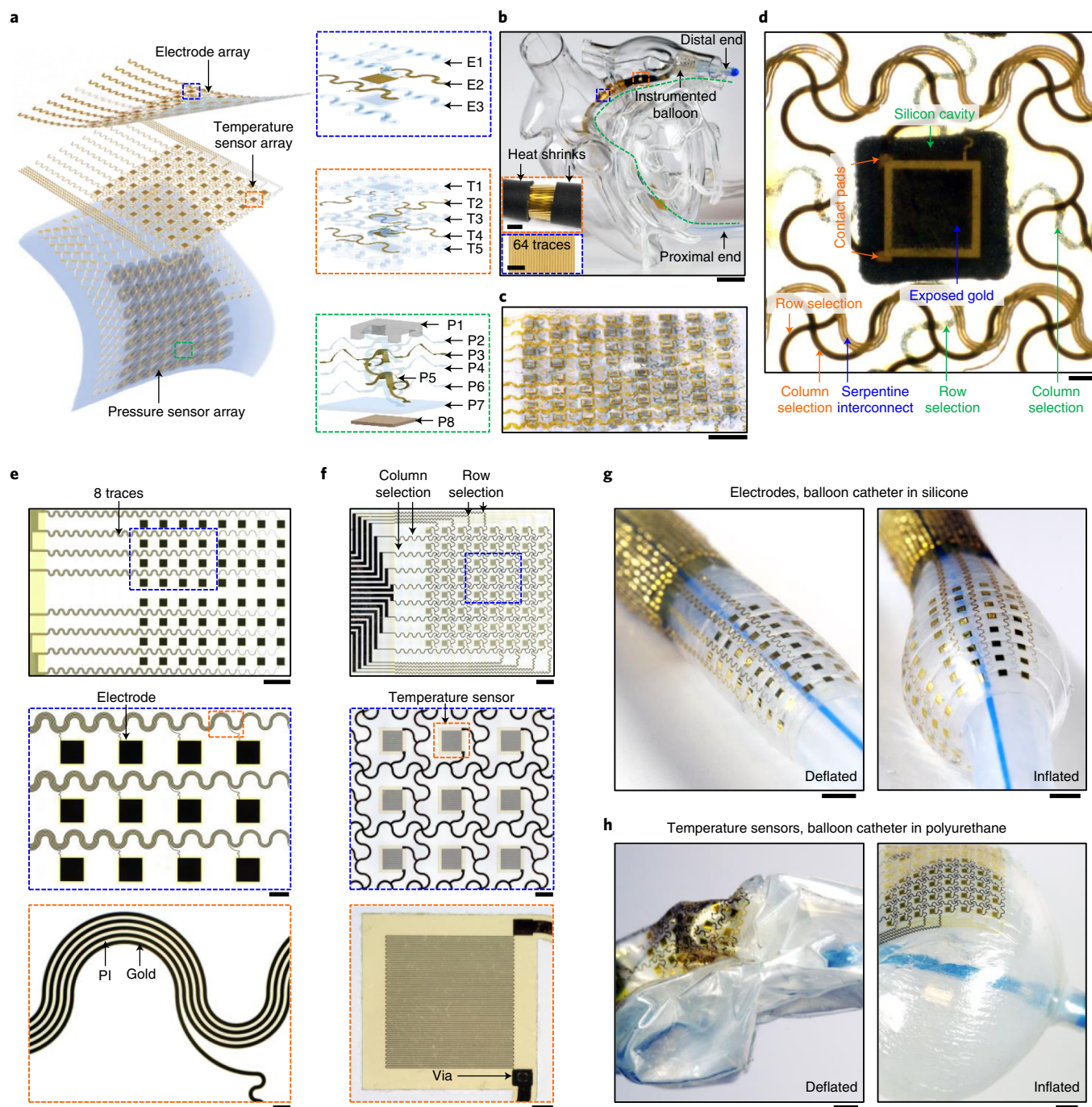
Fig. 1 | Multimodal, multiplexed soft sensors and actuators for minimally invasive surgery. a, Schematic illustration of the device arrays in a multilayer format. The top functional system allows electrophysiological mapping and RFA or IRE, with layers E1 (the top polymer film with openings), E2 (the array of electrodes and interconnects) and E3 (the bottom polymer film) for the electrode array. The next system enables measurements of temperature distributions, with layers T1 (the top polymer), T2 (the array of temperature sensors and row selection lines), T3 (a polymer interlayer with via openings), T4 (the column selection lines) and T5 (the bottom polymer film). The bottom system supports measurements of pressure distributions, with layers P1 (the array of silicon cavities), P2 (the top polymer film), P3 (the array of pressure sensors and row selection lines), P4 (a polymer interlayer with via openings), P5 (the column selection lines), P6 (the bottom polymer film), P7 (a layer of silicone elastomer) and P8 (an array of rigid islands). **b**, Image of an inflated, instrumented balloon catheter inserted into a transparent heart model. The green dashed curve illustrates the path of the catheter. Scale bars, 1 cm (main image); 2 mm (inset). **c**, Image of the vertically stacked arrays of electrodes, temperature sensors and pressure sensors. Scale bar, 2 mm. **d**, Image of one unit of the stacked arrays. Arrows and text in blue, orange and green correspond to layers for electrodes, temperature sensors and pressure sensors, respectively. Scale bar, 200 μm. **e,f**, Images of the array of electrodes (**e**) and array of temperature sensors (**f**) in planar format. **g**, Images of the array of electrodes transferred onto a balloon catheter of silicone. **h**, Images of the array of temperature sensors transferred on a balloon catheter of polyurethane. Scale bars in **e**–**h**, 2 mm for the images in black squares, 500 μm for images in blue outline, 100 μm for images in orange dashed outline.

by introducing a separate layer of thermal actuators (~3 mm² in area and 4 kΩ in resistance) (Supplementary Fig. 25). Here, transient plane source analysis of the time-domain temperature profiles from the sensors yields thermal conductivities at different locations[23]. Assessments of other parameters, such as flow of blood and other biofluids and tissue hydration levels, are also possible through further analysis of the data[24,25].

Figure 1g,h and Supplementary Figs. 26–30 present images and the results of finite element analysis (FEA) of the mechanics associated with electrode and temperature sensor arrays integrated onto various curvilinear surfaces. The small lateral dimensions of the arrays (~1 × 1 cm) facilitate integration onto different types of minimally invasive balloon catheters, including those constructed in silicone (Bard Bardex Foley Catheter 14 Fr, mounted in its deflated state; Fig. 1g) and polyurethane (cryoballoon catheter, Medtronic, Arctic Front, mounted in its inflated state; Fig. 1h). Such fabrication and integration processes establish straightforward routes to broad classes of advanced surgical instruments that can deliver therapy and provide high-quality multifunctional sensing.

Pressure sensing from arrays of 3D mesostructures. Measurement of localized pressures represents another essential function of relevance to many procedures. In particular, high-fidelity mapping of electrophysiological signals in the left atrium requires good contact between the sensor and the cardiac tissue. Furthermore, RFA and IRE demand intimate interfaces and well-controlled pressures to define the lateral spread and depths of lesions[26,27]. Both cases could benefit from pressure sensors capable of measuring small forces at soft-tissue interfaces, outside of the scope of capabilities of traditional thin-film sensors. The approach introduced here exploits compressive buckling to transform traditional metal strain gauges into 3D shapes with high sensitivity to normal force and low effective modulus. These simple metal constructs can be fabricated easily and at low cost, with necessary performance and without the hysteresis behaviours that tend to dominate alternative designs that rely on conductive composites[28,29].

The layouts for arrays of metal strain gauges of this type use geometries and architectures similar to those of the temperature sensors, in which column and row selection occurs through serpentine interconnects across two different layers. The two terminals of each strain gauge (Au, 100 μm in thickness, 2 μm in width) adopt a unique cross-shaped geometry (~130 μm in ribbon width and ~900 μm in ribbon length) (Supplementary Figs. 31 and 32) to facilitate wiring for column and row selections. Compressive buckling with a biaxial strain of 20% converts the cross-shaped patterns into tent-like 3D mesostructures (~170 μm in height) and the serpentine interconnections into 3D helices (~210 μm in height) with exceptional stretchability[30] (Supplementary Fig. 33). As demonstrated here, this simple scheme yields an 8 × 8 array of pressure sensors with 3D helical interconnections, involving more than 400 bonding sites, more than 300 3D mesostructures and 64 3D pressure sensors in five layers of polymer and metal (Fig. 2a and Supplementary Figs. 34 and 35).

For mounting on balloon catheters, these pressure sensor arrays must be not only stretchable, but also robust in response to the extreme mechanical perturbations associated with catheter deployment and navigation through a sheath. Covering the 3D tent-like mesostructures with silicon cavities (Fig. 2b–d) protects the pressure sensors from various forces associated with these procedures, with additional design flexibility to control their sensitivity. Each cavity has lateral dimensions of ~0.84 × 0.84 mm, with 4 square pillars (0.16 mm in length, 170 μm in height) at the corners (Supplementary Fig. 36a,b). In addition, rigid PI islands (~0.84 × 0.84 mm in lateral dimension, 12.5 μm in thickness) selectively bonded to the bottom surface of the substrate (P8 in Fig. 1a and Supplementary Fig. 5) constrain the deformations of the tent-like 3D mesostructures

under stretching, while maintaining stretchability of the whole array, as verified by experimental and FEA results in Fig. 2e and Supplementary Fig. 37. Such configurations also render the pressure sensor insensitive to other types of mechanical deformations, such as bending and twisting (Supplementary Fig. 38). The stretchable features allow the pressure sensor array to conformally integrate with balloons and other soft curvilinear surfaces (Fig. 2c,d).

With this structural design, normal pressures applied to the cavity depress the 4 pillars into the underlying elastomeric substrate (Dragon Skin 10 slow, modulus 166 kPa, 470 μm in thickness), thereby deforming the 3D tent-like mesostructures. The result is an increase in compressive strains in the metal strain gauges, which in turn, reduces the resistances of the sensors (Fig. 2f). Adjusting the side lengths (S) of the pillars provides a means to tune the sensitivity. Specifically, reducing S increases the pressure as a result of an associated decrease in contact areas, thereby increasing the sensitivity and decreasing the linear response range (for example, reducing S from 0.24 to 0.12 mm improves the sensitivity by a factor of 1.7; Fig. 2g). Other options to adjust the sensitivity and the linear response range involve changing the shapes of the 3D mesostructures, the thicknesses of the polymer layers, and the thickness and modulus of the elastomeric substrate (Supplementary Fig. 39). The thicknesses of the top elastomeric layers (for example, those associated with the electrodes or temperature sensors), however, have no influence on the sensitivity (Supplementary Fig. 40), thus ensuring stable performance of the pressure sensors when stacking additional functional layers on top.

In vitro characterization of the pressure sensor array relies on the same data-acquisition system used for recording temperature data (Fig. 2h–k and Supplementary Fig. 36c–h). Calibration of the 64 pressure sensors with a commercial force gauge reveals 100% yield and good uniformity in the sensitivity (mean of 8.2×10^{-5} kPa^{-1} and s.d. of 7.8×10^{-6} kPa^{-1} under Gaussian fitting) (Fig. 2h and Supplementary Fig. 36c,d). An external pressure of 30 kPa leads to small changes in strain in the metal wires (from −0.12% to −0.24% on average) and small displacements of the silicon pillars (~10% of the thickness of the elastomer). These pressure profiles have linear responses ($R^2 > 0.996$ in linear regression) with minimal hysteresis effects (difference in $\Delta R/R < 0.014\%$) (Fig. 2i). The linear responses from 0 to 30 kPa match the relevant range of pressures for many surgical procedures (for example, catheter ablation, force from 0 to 0.5 N under a hemispherical catheter tip with a diameter of 3.5 mm, corresponding to a pressure range of 0 to 26 kPa)[26]. Time-domain fractional changes in resistance of the sensor and pressure curves measured with the commercial force gauge demonstrate high consistency in both dynamic (correlation coefficient >0.96) and static conditions (correlation coefficient >0.99) (Supplementary Fig. 36e,f). The pressure sensor shows negligible time delay compared with the commercial force gauge in response to unloading of pressure at rates of 50 mm s^{-1} (Fig. 2j), and exhibits similar responses ($\Delta R/R$ with a mean of 0.26% and s.d. of 0.009%) under cyclic loading and unloading (~5,000 cycles) at 30 kPa (Fig. 2k and Supplementary Fig. 36g). Besides the high linearity, low hysteresis and drift, fast response time and long-term stability, these sensors also exhibit mechanical robustness under biaxial stretching (strains up to 30%) and multiple cycles of uniaxial stretching (10,000 cycles, 20% strain) (Supplementary Fig. 36h).

Integrating the pressure sensor array onto a customized balloon catheter allows the system to be inserted through small openings with the balloon in its deflated state for spatiotemporal mapping of pressure generated once the inflated balloon makes contact with a target surface. In vitro experiments on a non-perfused pig heart demonstrate such capabilities. In this experiment, a thin layer of silicone (Ecoflex 0030, 100 μm in thickness) covers the 3D mesostructures and silicon cavities to eliminate the sharp edges that can potentially harm soft tissues. Figure 2l shows images of the catheter
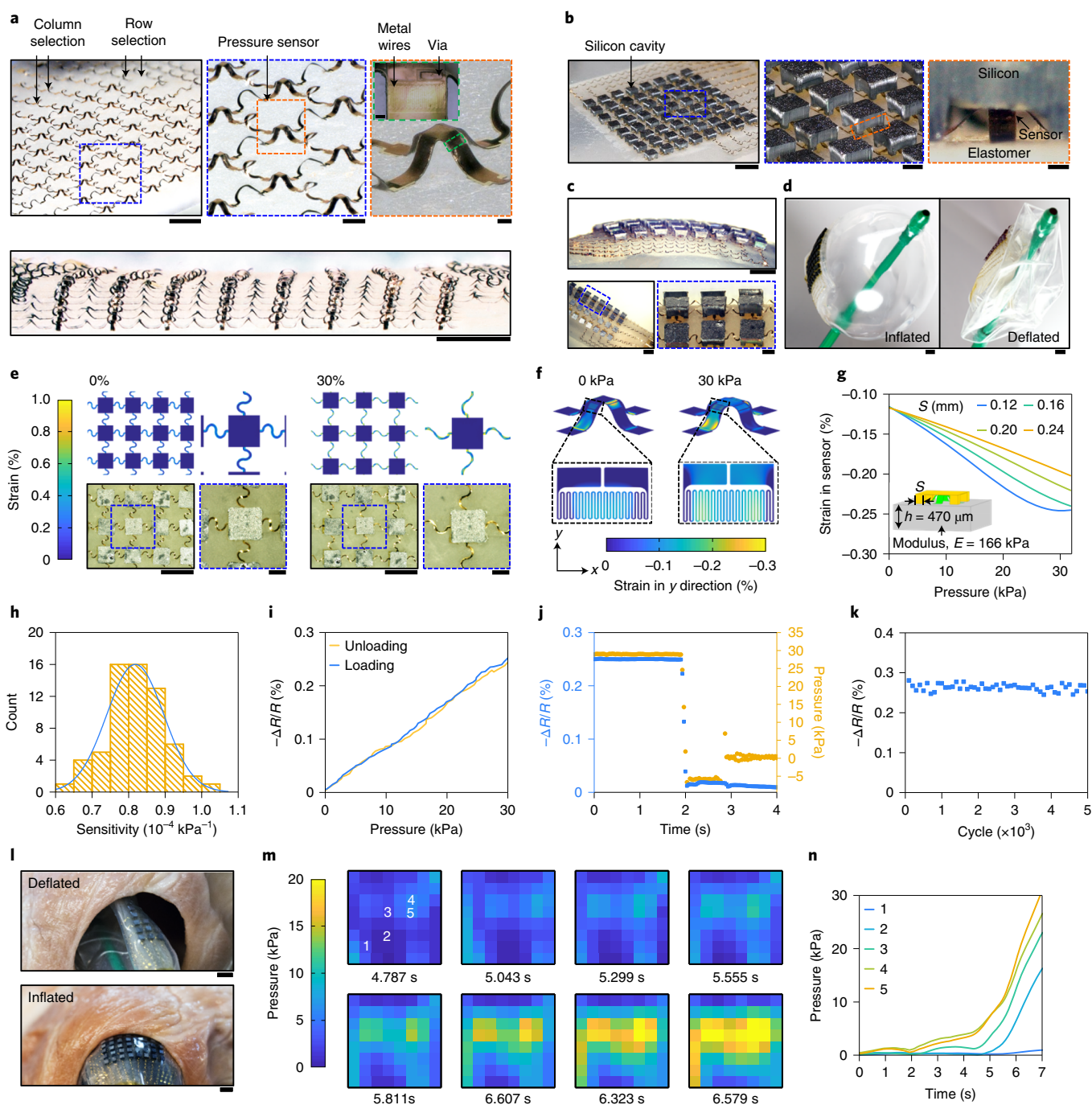
Fig. 2 | Design, assembly and characterization of the array of 3D pressure sensors. a, Images of the array before (**a**) and after (**b**) adding the silicon cavities. **c**, Images of the array transferred to curvilinear surfaces. **d**, Images of the array transferred on a customized balloon catheter. **e**, FEA results (top) and images (bottom) of the array under biaxial strains of 0% and 30%. **f**, FEA results of the strain distribution in the Au of one sensor under pressures of 0 and 30 kPa. **g**, FEA results illustrating the influence of geometric parameters on the sensitivity. S is the side length of the silicon pillar, h is the thickness of the elastomer substrate and E is the modulus of the elastomer substrate. **h**, Histogram and Gaussian line-shape fitting of the sensitivity. **i**, Fractional change of resistance (R) of the sensor at different pressures during loading and unloading. **j**, Responses from the sensor (blue curve) and a commercial force gauge (orange curve) under fast unloading. **k**, Fractional change of resistance under 5,000 cycles of loading–unloading. **l**, Images of a customized balloon catheter equipped with an array of 3D pressure sensors inserted into a pig heart model. **m**, Spatiotemporal mapping of pressure during inflation of the balloon catheter on a pig heart. **n**, Time-domain pressure curves from five sensors. The numbers in **m** indicate the positions of the five sensors. Scale bars, 2 mm for the images in black outline, 500 μm for images in blue dashed outline, 100 μm for images in orange dashed outline, and 20 μm for the image in green dashed outline.

inserted into the left ventricle of the pig heart before and after inflation. During the process of inflation, the balloon expands, gradually contacting the endocardial surface as recorded with the pressure sensors. Figure 2m,n and Supplementary Video 2 show the pressure distributions on the balloon and the time-domain pressure curves recorded from different sensors during inflation.
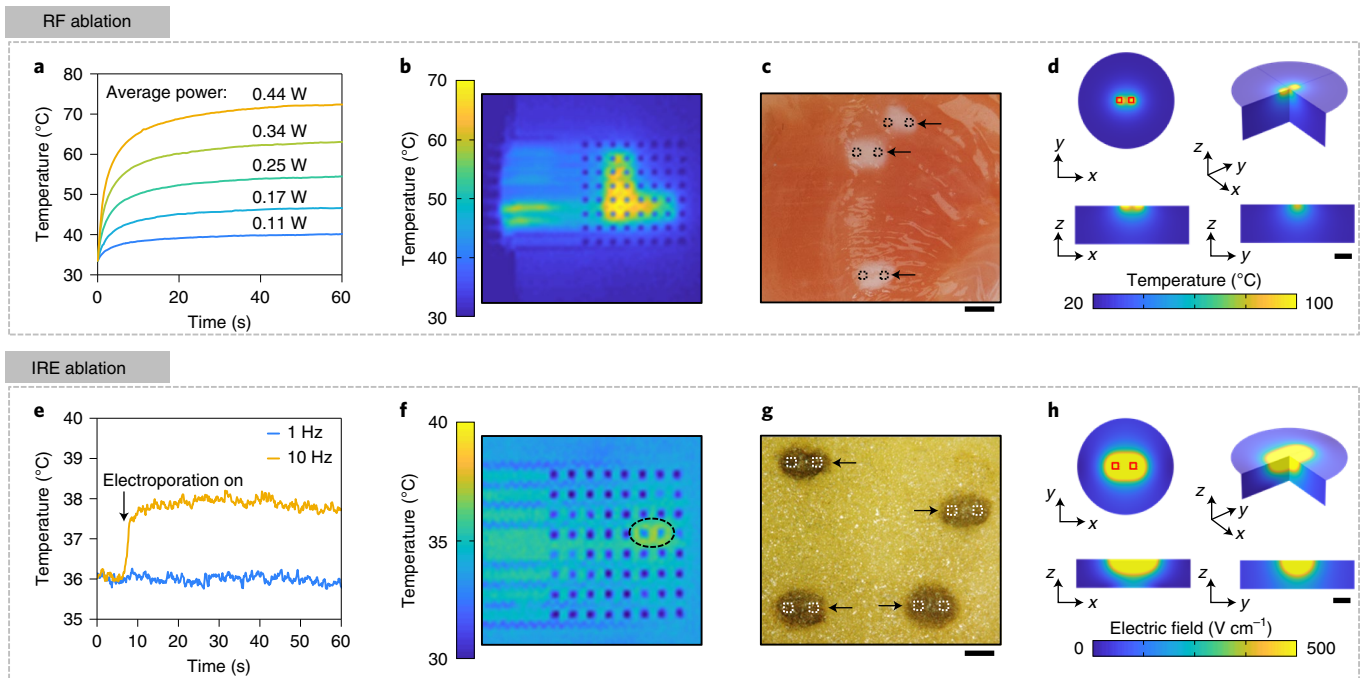
Fig. 3 | Therapeutic functions. a, Temperature profiles determined with sensors at the locations of electrodes during bipolar RFA with two adjacent electrodes at different input powers. **b**, A representative example of the temperature distribution during bipolar RFA (measured from an infrared microscope). Passing radiofrequency power to multiple electrode pairs yields an 'L' pattern. The ablation experiments in **a,b** use agar hydrogel (2 wt% agar, 98 wt% 0.1 M PBS) at 37 °C. **c**, Lesions created on a non-perfused tissue (chicken breast) by RFA. The black dashed squares illustrate the positions of the electrodes for ablation. Scale bar, 2 mm. **d**, FEA results for the 3D temperature distributions during RFA. Red solid squares in the top left frame indicate the positions of the electrodes. Scale bar, 2 mm. **e**, Temperature profiles determined with sensors at the locations of the electrodes during IRE at frequencies of 1 Hz and 10 Hz. **f**, Temperature distribution during IRE at 10 Hz (measured with an infrared microscope). The black dashed circles indicate the electrodes with applied radiofrequency power. **g**, Lesions created on a vegetable model (potato) with IRE (1 Hz, 20 s). The white dashed squares illustrate the positions of the electrodes for IRE. Scale bar, 2 mm. IRE in **e–g** uses biphasic pulses with amplitudes of ~200 V and durations of 100 μs. **h**, FEA results for the 3D electric field distributions during IRE. The red solid squares in the top left frame indicate the positions of the electrodes. Scale bar, 2 mm.

Therapeutic functions and simultaneous, multimodal operation. The collection of multimodal, multiplexed sensing capabilities reported here creates many options in advanced, high-density and multifunctional diagnostics. Therapeutic functions are also possible by delivering different types of electrical signals to the biology through the system. One example involves sinusoidal inputs (frequency of 400–500 kHz, Supplementary Fig. 41) to selected electrodes in the array for RFA therapy—currently the most widely used procedure to terminate arrhythmias—via electrical currents and associated Joule heating in the adjacent tissues. For characterization purposes, ionic conductive hydrogel (2 wt% agar, 98 wt% 0.1 M phosphate-buffered saline (PBS)) stands in for the tissue. Figure 3a shows the time-domain profile of the maximum temperature during bipolar RFA, in which all 64 electrodes in the array contact the hydrogel and radiofrequency signals pass only to two adjacent electrodes, at different powers (from ~0.1 to ~0.4 W, corresponding to current densities from ~38 to ~77 mA mm^{-2}). The array format enables spatially programmable RFA by applying power to selected electrodes (Fig. 3b and Supplementary Figs. 42–45). Advantages include capabilities for (1) creating lesions at different positions without moving the array (top frames in Supplementary Fig. 42a,b), and (2) forming a series of lesions with programmable shapes and dimensions such as an 'L' pattern (Fig. 3b), separate lesions at multiple locations, and large-area lesions (bottom frames in Supplementary Fig. 42a,b). Such features may provide an attractive alternative to the traditional means for creating lesions in a point-by-point manner by manually steering a catheter tip with only a single pair of exposed electrodes[31].

The same process can apply to non-perfused biological tissues (Fig. 3c and Supplementary Figs. 46–49). Figure 3c shows an image

of chicken breast after simultaneous, multisite bipolar ablation. Three lesions appear as white regions, marked with black dashed squares, as a demonstration of the ablation functionality. Additional results, including ablation based on monopolar configurations, yield lesions with lateral dimensions from 0.5 to 10 mm and depths from 0.2 to 3.2 mm (Supplementary Figs. 46–49). FEA models can capture the 3D distributions in temperature for these cases (Supplementary Figs. 43, 46, 47 and 49–57). Figure 3d presents an example of bipolar ablation. An alternating voltage of 33.6 V at a frequency of 400 kHz applied to two adjacent electrodes leads to temperatures that reach the highest values in the areas near the electrodes, and gradually decrease with distance from the electrodes (parameters listed in Supplementary Table 2). Additional FEA results indicate that precise control of the dimensions of the lesions are possible by adjusting the geometrical parameters of the electrode array (Supplementary Note 2 and Supplementary Figs. 54–57).

Different types of input signals enable additional modes of therapy. For example, application of a series of high-voltage pulses to a pair of electrodes enables IRE ablation, the latest US Food and Drug Administration-approved method for treating arrhythmias. In this process, pulsed electric fields (>500 V cm^{-1}) increase cell permeability, thereby causing cell death and termination of aberrant rhythms, typically without substantial heating. Figure 3e–h and Supplementary Figs. 58–65 demonstrate the capabilities of the electrode array for IRE. This approach exploits electrical mechanisms of cell death without the side-effects of thermal processes, for enhanced safety and improved confinement of lesion formation. The results also exhibit improved tissue specificity, and reduced potential for collateral damage and thrombus formation compared

with RFA[32]. An infrared microscope can capture the temperature profiles (Fig. 3e) during IRE from biphasic voltage pulses with amplitudes of ~200 V and durations of 100 μs (Supplementary Fig. 58a). Pulses at a frequency of 10 Hz (Supplementary Fig. 58b) cause a temperature rise of only ~2 °C (Fig. 3e,f). Advantages of IRE through a high-density electrode array include reductions in the voltages necessary to generate sufficient electric fields between adjacent electrodes, options in spatially programmable patterns of IRE and relatively uniform electric field lines, as required by pre-clinical studies.

In vitro experiments on a vegetable (potato) model (Fig. 3g and Supplementary Figs. 60–62) and FEA results (Fig. 3h and Supplementary Figs. 63–65) verify these advantages. IRE on a potato can damage the membranes of the cells under high electric field to release phenoloxidase enzyme. The enzyme then promotes the oxidation of phenolic compounds to yield dark regions[33]. Experiments that exploit these effects involve a set of twenty biphasic voltage pulses (amplitudes of ~200 V and durations of 100 μs) at a frequency of 1 Hz applied to two adjacent electrodes in contact with a potato. The dark lesions become visible 12 h after IRE (Fig. 3g). Lesions arranged in an 'L' pattern demonstrate the programmability supported by the addressable electrode array (Supplementary Fig. 60). The small spacings between the electrodes (1 mm) enable formation of lesions at relatively low voltages (~100 V; Supplementary Fig. 61). The voltages required to form lesions depend, theoretically, on the spacing of electrodes, in a manner consistent with the electric field distributions from coplanar electrodes[34]. For a given voltage, electrodes with smaller spacings create deeper lesions in most cases, but the relationship follows a non-trivial functional form. Supplementary Note 3 and Supplementary Fig. 63 show these scaling relationships. On the basis of analytical approximations, the depths of the lesions (d) correspond to the maximum value of d that satisfies

$$\frac{V_0}{2K(L,S)} \frac{\frac{L-S}{2}}{\sqrt{\left(\frac{(L-S)^2}{4} + \frac{(L-S)^2}{(L+S)^2} d^2\right)\left(\frac{(L-S)^2}{4} + d^2\right)}} > E_{thres} \quad (1)$$

where V_0 is the applied potential to the electrodes, L is the distance between the centres of two electrodes, S is the side length of the electrodes, $K(L,S)$ is the elliptic integral (equal to $\int_0^{\pi/2} \frac{d\theta}{\sqrt{1-\left(\frac{L-S}{L+S}\sin\theta\right)^2}}$), E_{thres} is the electric field intensity required to form lesions. Assigning parameters used in the experiments ($V_0 = 200$ V, $L = 1.5$ mm, $S = 0.5$ mm, $E_{thres} = 500$ V cm^{-1}) to equation (1) yields lesion depth of ~0.75 mm, comparable with the experimental results (~0.60 mm) (Supplementary Fig. 61). These features may allow termination of arrhythmias with voltages lower than those (3,000 V) used in recent preclinical cardiac studies with conventional electrodes[32]. FEA results in Fig. 3h and Supplementary Figs. 64 and 65 demonstrate good agreement with experimental results. These models provide a means to examine the lesions in 3D and to predict the dimensions of the lesions under different conditions.

Such therapeutic functions (that is, RFA and IRE) and capabilities in electrophysiological and functional mapping offer some advantages over commercial catheter devices, such as high spatial and temporal resolution, relatively low power and voltage thresholds to achieve effective therapies, and multimodal capabilities on a single system to obviate the need for multiple catheters (Supplementary Table 3). Combining these diagnostic and therapeutic functions also creates possibilities for interventions guided, in real-time, by multifunctional sensor feedback. Figure 4a–d shows temperature mapping during RFA as a demonstration of the simultaneous operation of the arrays of electrodes and temperature sensors. Here, the array of temperature sensors bonds to the bottom surface of the electrode

array with a thin layer of PI (~1.5 μm thick) (Fig. 4a, left), to offer small thickness, strong adhesion and excellent thermal and physical contact for precise temperature measurements during ablation. By comparison, bonding the temperature sensors to the electrodes through a layer of silicone (Ecoflex, ~100 μm thick, right) results in reduced measurement accuracy. Figure 4b compares the temperature profiles measured from systems built with these two bonding strategies during RFA on hydrogel (2 wt% agar, 98 wt% 0.1 M PBS, 37 °C). Results of FEA (Supplementary Note 4 and Supplementary Fig. 66) yield detailed information on the relationships between the temperature and the thickness of the interlayer, the thermal resistance at the interface and the thermal properties of the constituent materials. Spatiotemporal mapping of temperature can further enrich the information for improved control. Figure 4c,d and Supplementary Fig. 67a present the spatial distributions of temperature and the time-domain temperature profiles recorded from different sensors during bipolar RFA with two adjacent electrodes on hydrogel (2 wt% agar, 98 wt% 0.1 M PBS, 37 °C). Such results can potentially provide insights during ablation therapy to improve control over the process.

Pressure sensors in this multimodal electronic system can operate in conjunction with electrodes and temperature sensors for both diagnostic and therapeutic functions. Here, non-perfused tissues immersed in 1 M PBS serve as the targets to simulate in vivo conditions. The impedances between the two electrodes that contact the tissue, in this case, increase with the applied pressure (measured by the pressure sensors) (Fig. 4e and Supplementary Fig. 67b), due to a reduction in the amount of PBS at the interface. Compared with traditional tip or ring electrodes for ablation, the planar electrodes and soft, stretchable substrates used here can adapt to the surfaces of the tissues. This contact reduces the pressures required to eliminate fluids at the interface, thereby enhancing the thermal dissipation into the tissues rather than adjacent biofluids[35]. Figure 4f presents a series of lesions created through bipolar RFA under different pressures (from 0 to 30 kPa, measured from the pressure sensors). At low pressures, radiofrequency energy is mostly delivered to the PBS. Thermal conduction through the PBS transfers heat to the surface of the tissue, resulting in lesions with comparatively large, poorly controlled lateral dimensions (ellipse with major axis of ~3.2 mm and minor axis of ~2.4 mm) and small depths (~0.65 mm).

The temperature and pressure sensors both rely on resistance changes in thin metal wires. Minimizing interference across these different sensors is important. The arrays of temperature sensors adopt a planar configuration to avoid substantial geometric changes under normal pressure. These sensors can yield calibration factors to account for the effect of temperature on the pressure sensors. An alternative way to reduce the effects of temperature sensitivity of the pressure sensors is to replace thin wires of Au with copper–nickel alloy (constantan (Cu$_{55}$Ni$_{45}$)), which has a similar strain-gauge factor (~2) but a much smaller TCR compared with Au[36,37]. Sputtering of constantan at room temperature and 100 °C yields sensors with TCRs of −40 and 9.8 ppm K^{-1}, respectively (Fig. 4g). The temperature sensitivities are around 40 and 170 times, respectively, smaller than those from the arrays of temperature sensors based on Au. Similar procedures enable the fabrication of 3D pressure sensors in constantan in parallel fashion (Fig. 4h and Supplementary Note 5). The constantan pressure sensors can effectively detect normal pressure and integrate with other electronic devices to enable simultaneous RFA, temperature sensing and pressure sensing (Fig. 4i and Supplementary Fig. 67c,d).

Ex vivo studies on Langendorff rabbit and human heart models. Experiments on Langendorff rabbit heart models validate the diagnostic and therapeutic functions of the instrumented balloon catheters. Electrograms and corresponding voltage maps recorded from the epicardial surface of a rabbit heart using the electrode array
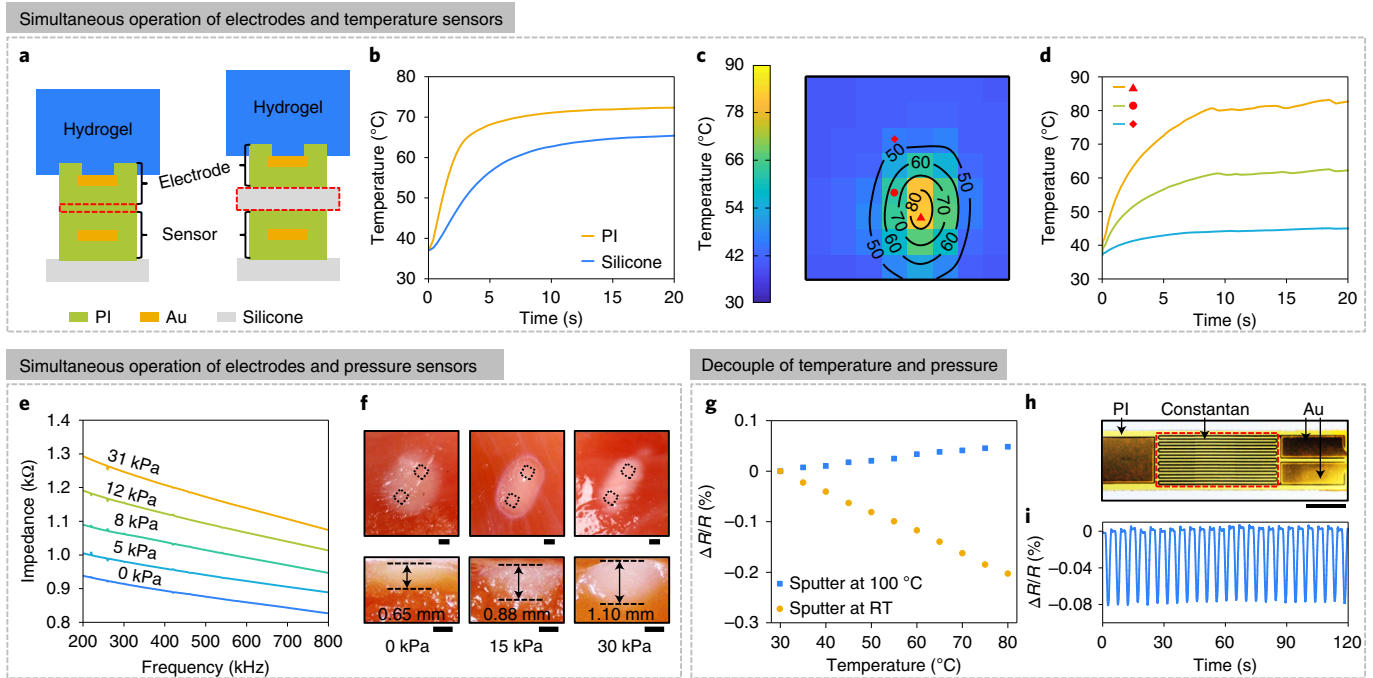
Fig. 4 | Simultaneous, multimodal operation. a, Schematic of the side view of the stacked electrode and temperature sensor with PI (left) and silicone (right) as the interlayer. **b**, Temperature profiles during RFA measured from temperature sensors with PI (1.5 μm thick) and silicone (Ecoflex, 100 μm thick) as the interlayer between the sensor and the ablation electrodes. **c**, Temperature distribution at 20 s after initiating ablation during bipolar RFA (measured from the temperature sensor array). Computation of the isotherms relies on a four-order 2D interpolation of the raw data. **d**, Time-domain temperature curves from three temperature sensors. The ablation experiments in **a–d** use agar hydrogel (2 wt% agar, 98 wt% 0.1 M PBS) at 37 °C. **e**, Impedance spectra of the electrode when in contact with a non-perfused tissue (chicken breast immersed in 0.1 M PBS) at different pressures. **f**, Lesions created on non-perfused tissues at different pressures. Top (top) and side (bottom) views of the lesions. The black dashed squares illustrate the positions of the electrodes for ablation. Scale bars, 0.5 mm. **g**, Fractional change of resistance (*R*) of resistors formed with constantan sputtered at 100 °C and room temperature. **h**, Image of a sensor formed in constantan and Au. Scale bar, 100 μm. **i**, Fractional change of resistance of the pressure sensor in constantan under periodic pressure of 20 kPa.

during both paced activation pattern and arrhythmia highlight electrical sensing capabilities (Fig. 5a–c, Supplementary Figs. 68–72 and Supplementary Video 3). The results correspond to placement on the left posterior ventricular surface of the rabbit heart (Fig. 5a). Representative electrograms show the ability to detect atrial excitation (P wave), ventricular excitation (QRS wave) and ventricular relaxation (T wave) (Fig. 5b). Voltage maps for selected time points (indicated by the dashed lines in Fig. 5b) illustrate sensing of the excitation wave (time points 2 and 3) as it propagates along the ventricular surface (Fig. 5c).

IRE and RFA testing show the efficacy of the technology in therapy. In IRE, a pair of electrocardiogram (ECG) electrodes records signals during the process (Fig. 5d). Initially, the rabbit heart rate is in sinus rhythm. Application of IRE (biphasic electric pulses with amplitudes of ~200 V, duration of 100 μs and frequency of 50 Hz) immediately induces an arrhythmia. After ~ 46 s, the arrhythmia terminates spontaneously, and the heart exhibits sinus rhythm again. RFA therapy enables the creation of lesions on the epicardial surface (Fig. 5e). In this case, the thin, soft electronics offer two advantages over conventional rigid devices. First, the electrode array for RFA forms an intimate, conformal contact to the cardiac surface, with minimal exposed area to the surrounding blood, thereby reducing the undesired resistive heating outside of the tissue (Supplementary Fig. 73). Second, the temperature sensor array, located below the electrode array and separated with only a thin layer of PI (~1.5 μm in thickness), accurately records the temperature with capability for use in feedback control of the ablation. Figure 5f,g and Supplementary Video 4 demonstrate the spatiotemporal distributions of temperature during RFA. The two temperature

sensors that correspond to the two electrodes for RFA exhibit the highest temperature increments, as expected.

The vertically stacked arrays of electrodes and pressure sensors enable synchronized multimodal measurements of electrograms and pressure. Figure 5h,i presents results during both sinus rhythm and under pacing conditions. The amplitudes of the electrograms recorded from the electrodes range from 1 to 3 mV and depend on the contact pressure. Poor contacts between the electrodes and the cardiac tissue, corresponding to low pressures, result in reduced amplitudes (blue curves in Fig. 5h, left). At a contact pressure of ~16 kPa, the sensors detect subtle contractions of the rabbit heart, as indicated by the peaks and valleys in plots of the time dependence of the pressure (green curves in Fig. 5h, left). The synchronized signals of electrogram and pressure afford opportunities to investigate correlations between the electrical and mechanical behaviours of cardiac tissues (Fig. 5h, right). Further increasing the contact pressure locally restricts the movement of the heart, and the pressure sensor in this case yields nearly constant values without obvious peaks and valleys (orange curves in Fig. 5h, left). In this case, the mechanical stress impairs the cardiac activity and results in lower overall amplitude of electrograms.

Experiments on the endocardial surface of an ex vivo donor human heart LV wedge model further validate the multifunctional capabilities and highlight the fidelity in electrogram mapping (Fig. 6, Supplementary Figs. 74–78 and Supplementary Video 5). Placing the electrode array on the endocardial surface of the left ventricle (Fig. 6a,b) yields electrograms and the ability to detect ventricular excitation and repolarization wavefronts (Fig. 6c). The voltage maps involve selected time points (indicated by the dashed
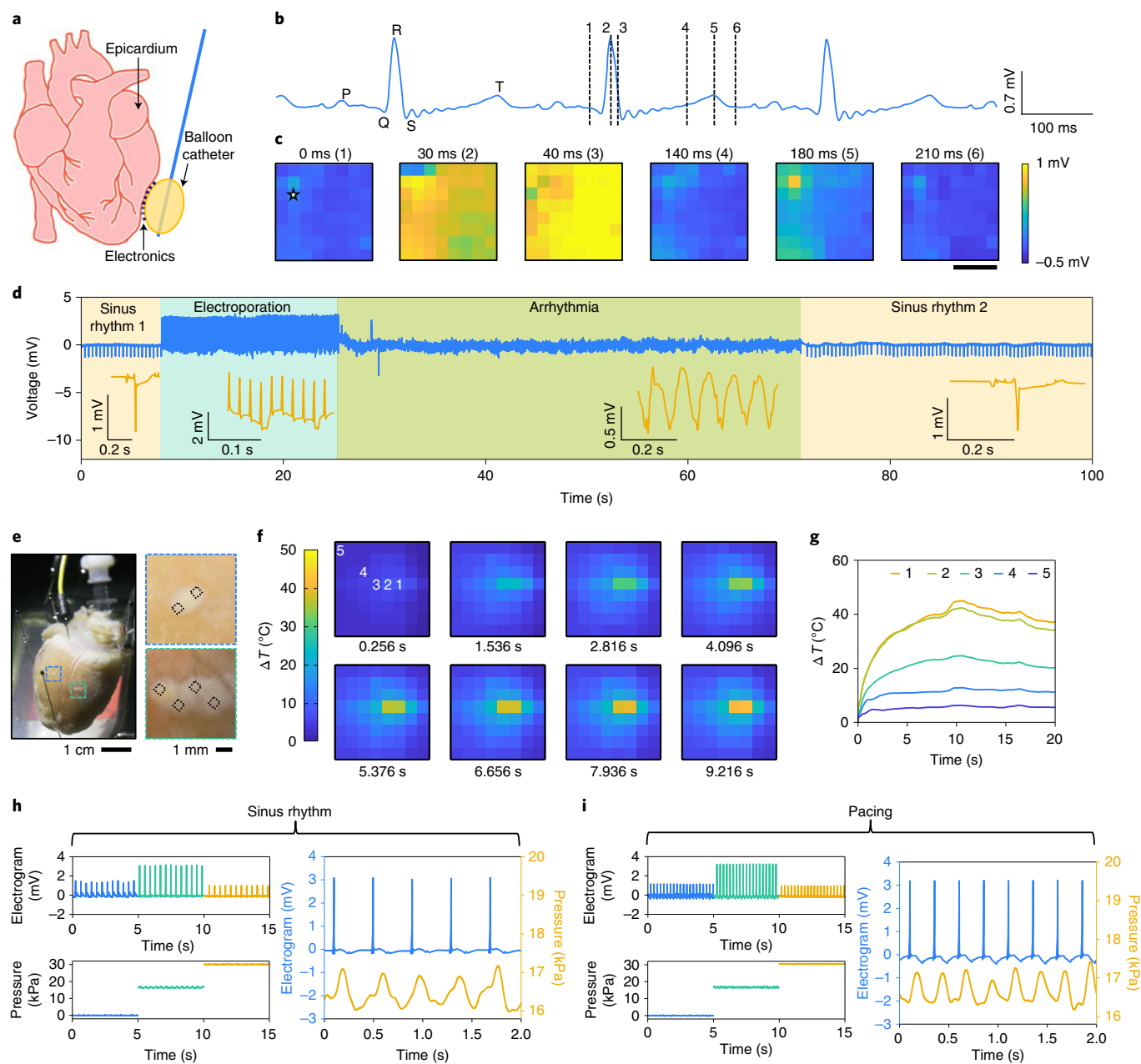
Fig. 5 | Multifunctionality of instrumented balloon catheters demonstrated with Langendorff rabbit heart models. a, Schematic of the test setup. **b**, A single trace electrogram measured from the electrode array under pacing (200 beats per min (BPM)). **c**, Voltage-mapping data at different time points (indicated by the black dashed lines in **b**). The star indicates the pixel that corresponds to the trace in **b**. Scale bar, 5 mm. **d**, ECG of the rabbit heart recorded before, during and after IRE at a frequency of 50 Hz. Insets, magnified time-domain curves. **e**, Lesions created on the epicardial surface of a rabbit heart through bipolar RFA. The black dashed squares illustrate the positions of the electrodes for ablation. **f**, Spatiotemporal temperature mapping during bipolar RFA on a rabbit heart (measured from the temperature sensor array). **g**, Time-domain temperature curves from five temperature sensors. The numbers in **f** indicate the positions of the five temperature sensors. **h,i**, Simultaneous electrogram and pressure recording during sinus rhythm (**h**) and pacing (**i**). **h,i**, Left: electrograms under different contact pressures between the balloon catheter and the rabbit heart. **h,i**, Right: magnified time-domain curves of the electrograms and pressure at contact pressures of ~16 kPa (right).

lines in Fig. 6c) to highlight sensing of the excitation wave (time points 2 and 3) and the repolarization wave (time point 5) propagating along the endocardial surface (Fig. 6d).

Representative time-aligned optical and electrical signals recorded from the left ventricle surface highlight the ability to record data consistent with that captured using an optical mapping modality (Fig. 6e–k) through electrograms and optical action potentials (OAPs) recorded from the endocardial surface. Representative time-aligned electrograms and OAPs from three distinct locations,

highlighted by the blue, green and red stars in Fig. 6e, correspond to two different heart rates (30 and 60 BPM) (Fig. 6f). The features extracted from the OAPs and the electrograms include the activation time and the action potential duration (Fig. 6g). The activation time corresponds to the maximum upstroke on the OAP, and the minimum slope on the electrogram. The action potential duration (APD50) on the OAP corresponds to the time point when the tissue has relaxed by 50%; for the electrogram, this time corresponds to the maximum slope on the T wave. The optical activation maps
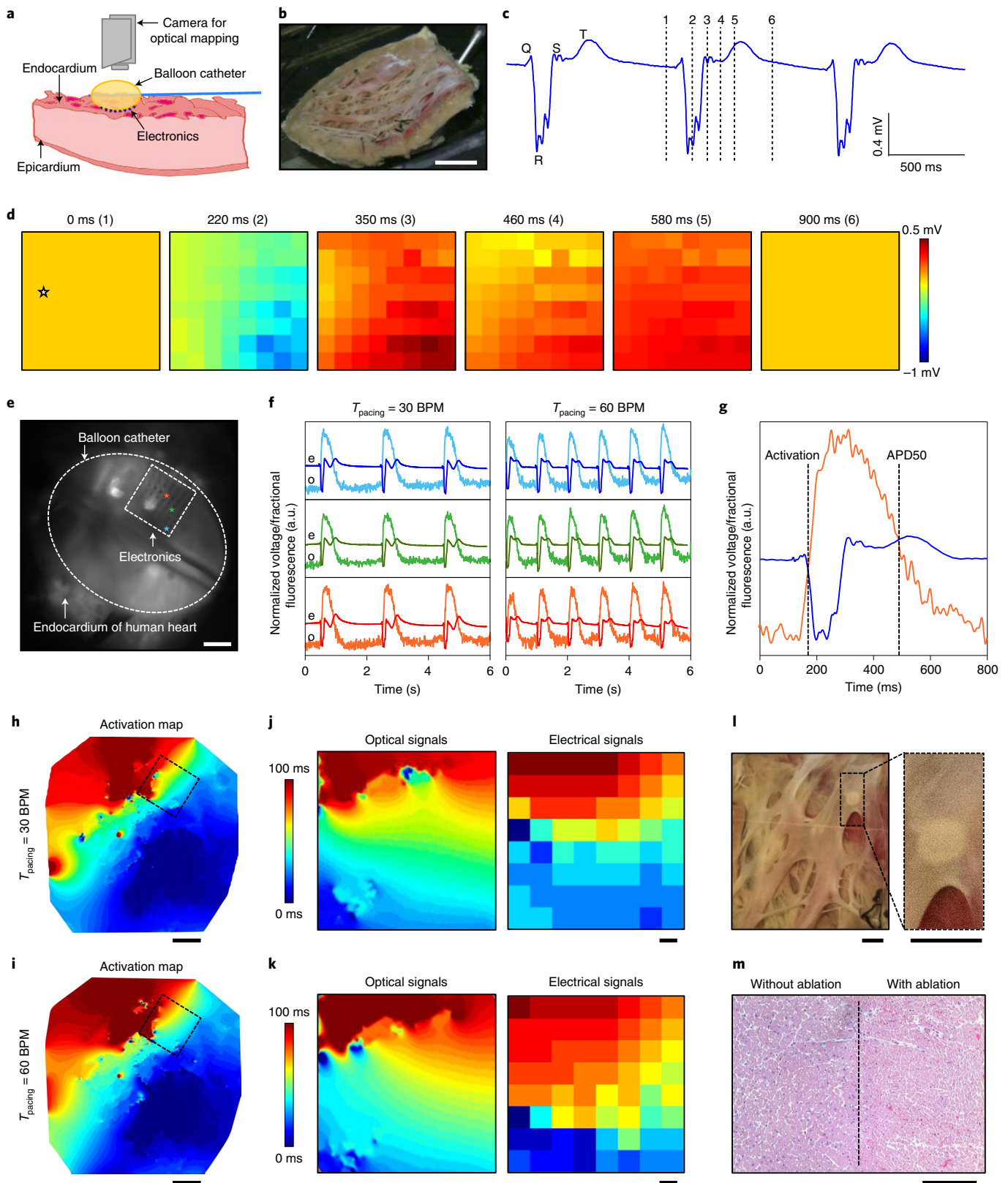
at 30 BPM (Fig. 6h) and 60 BPM (Fig. 6i) and the corresponding electrical activation maps at 30 BPM (Fig. 6j) and 60 BPM (Fig. 6k) show strong correlations. Slight discrepancies result from the different sensing mechanisms. Optical signals average electrical activity over the depth (~4 mm, associated with diffusion of the voltage-sensitive dye) of the tissue, whereas the electrodes record signals from the tissue surface that is in proximity with the myocardium.

The electrode array can also ablate the tissue to create lesions that can be examined using immunohistology (Fig. 6l,m). Visual examination of the ablated region shows a lesion 3 mm in diameter and 2 mm deep (Fig. 6l). Histological evaluation in Fig. 6m indicates

Fig. 6 | Endocardial electrophysiological studies on Langendorff human heart models. a, Schematic of the setup for synchronized optical and electrical mapping. **b**, Image of the endocardial surface of a human ventricle. Scale bar, 15 mm. **c**, A single trace electrogram measured from the electrode array under pacing (60 BPM). **d**, Voltage-mapping data at different time points (indicated by the black dashed lines in **c**). The star indicates the pixel that corresponds to the trace in **c**. **e**, Image from the camera for optical recording (with a 700 nm long-pass filter, under 655 nm excitation light; further details in Methods). The white dashed ellipse indicates the position of the instrumented balloon catheter. The white dashed square indicates the position of the electrode array. Scale bar, 5 mm. **f**, Representative optical (o) and electrical (e) signals from three different locations (marked with stars in **e**). a.u., arbitrary units. **g**, Comparison of the optical (orange curve) and electrical (blue curve) signals in one cycle. **h,i**, Activation maps of the human heart left ventricle wedge calculated from the optical data. Scale bars, 1 cm. **j,k**, Activation maps obtained from the optical and electrical data for regions inside the black dashed squares in **h** and **i**. Scale bars, 1 mm. **l**, Images of the lesion created on a human heart. Scale bars, 5 mm. **m**, Histology of the lesion created on a human heart. Scale bar, 200 μm.

that the region with RFA (right) has a reduced number of nuclei (blue dots). The balloon-mounted systems offer better control of the locations of the electrodes and lesions compared with other flexible arrays based on ultrathin films, open mesh designs or filamentary probes, due to the random deformations of the latter systems after implantation. Relatively small uncertainties of the shapes of the inflated balloons (within 10% of the target shape[38], <0.6 mm in distance for the balloon used here) are acceptable for ablation therapies in humans, where the total lateral dimensions of the lesions range from several millimetres to centimetre scale. These results suggest the possibility of using the instrumented balloon catheter as an advanced surgical tool for the diagnosis and treatment of heart disease in humans.

Discussion

The results presented here address fundamental limitations of conventional cardiac devices—modulus mismatch between the devices and cardiac tissues and insufficient modalities and spatial densities in sensing and actuation—through a collection of soft, multiplexed electronic systems in multilayered configurations. Integration of such systems with commercial and/or customized catheters yield sophisticated systems with capabilities in conformal, high-density and multimodal sensing and actuation. In vitro testing, together with computational studies and evaluations in rabbit and human hearts, demonstrates advantages over conventional cardiac devices in form factor, functionality, and programmability. Key advances involve (1) the capabilities in high-density multifunctional mapping using devices that adopt both 2D and 3D designs, (2) multilayer, modular layouts that provide scalable paths to technologies with customizable diagnostic and therapeutic functions, and (3) the simultaneous, multimodal operation of arrays of sensors and actuators, with potential for closed-loop control. These features promise to enable physicians to acquire a rich set of physiological information and to complete surgeries in shorter times with a single instrumented-catheter system. The integration strategy can apply to other surgical instruments relevant to procedures on various parts of the nervous system, urinary system, gastrointestinal tract and elsewhere. These concepts may therefore form a starting point for further developments of advanced surgical devices capable of minimally invasive interactions with the human body.

Methods

Fabrication of the electrode array. Fabrication of the electrode array began with spin coating a layer of PI (PI2545, 3.3 μm in thickness) on a silicon wafer with Ti/Cu (10 nm/100 nm in thickness) as the sacrificial layer. Subsequent lift-off processes defined the pattern of metal electrodes and serpentine connections (Cr/Au, 10 nm/300 nm in thickness). Spin coating another layer of PI (PI2545, 3.3 μm in thickness) covered the metal pattern. Deposition of SiO$_2$ (100 nm in thickness) created a layer of material for a hard mask. Photolithography and dry etching of the SiO$_2$ and oxygen plasma etching (March RIE) of PI yielded the outline of the electrode array. Removing the top layer of Cu and undercutting the bottom layer of Cu allowed transfer of the electrode array from the silicon wafer to a water-soluble tape.

Fabrication of the temperature sensor array. Fabrication of the temperature sensor array started with spin coating a layer of PI (PI2545, 3.3 μm in thickness)

on a silicon wafer with Ti/Cu (10 nm/100 nm in thickness) as the sacrificial layer. Lift-off processes defined the patterns for the temperature sensors and serpentine connections for row selection in Cr/Au (10 nm/100 nm in thickness). Another layer of PI (PI2545, 1 μm in thickness) covered the metal pattern. Photolithography (AZ4620, 10 μm in thickness) and oxygen plasma etching (March RIE) defined vias through the PI at appropriate locations. Sputter deposition of Cr/Au (10 nm/100 nm in thickness) coated the exposed regions as well as the side walls of the vias with metal. Photolithography and wet etching of Cr/Au yielded the serpentine connections for column selection. Spin coating another layer of PI (PI2545, 1 μm in thickness) covered the metal pattern for column selection. Deposition of Cu (100 nm in thickness) yielded a hard mask for dry etching of the PI. Photolithography and wet etching of the Cu, and oxygen plasma etching (March RIE) of the PI formed the outline of the temperature sensor array. Removing the top layer of Cu and undercutting the bottom layer of Cu allowed transfer of the temperature sensor array from the silicon wafer to a water-soluble tape. Deposition of SiO$_2$ (100 nm in thickness) on the tape through a shadow mask and subsequent UV ozone treatment of the SiO$_2$ surface and of a layer of silicone enabled bonding of the temperature sensor array to the silicone elastomer.

Fabrication of the pressure sensor array. Fabrication of the Au-based pressure sensor array began with the same procedures used for fabricating the temperature sensor array. After transferring the array onto water-soluble tape, deposition of SiO$_2$ (100 nm in thickness) through a shadow mask defined the bonding regions. UV ozone treatment of a prestretched silicone elastomer and of the SiO$_2$ surface created hydroxyl termination on the surfaces for bonding. Attaching the 2D precursor to the pressure sensor array onto the stretched elastomer, followed by heating (70 °C, 10 min), dissolving water-soluble tape, and releasing the prestrain, yielded the final 3D configuration. Laser cutting (LPKF ProtoLaser R) and assembling the silicon cavities and PI islands on the top and bottom surfaces completed the fabrication. Fabrication of the constantan-based pressure sensor array followed similar procedures but with the row selection lines (Au) and the sensors formed in two separate steps of lithography, as described in Supplementary Note 5.

Multilayer integration. The process for stacking multiplexed arrays exploited a polydimethylsiloxane stamp with patterns of relief configured to selectively deliver uncured PI (spin coat at 3,000 rpm) as an adhesive layer. A transfer printing machine aligned the temperature sensor array on silicone with the electrode array on water-soluble tape, with uncured PI as the adhesive layer. Curing the PI and removing the tape completed the stacking process. UV ozone treatment of the bottom surface of the temperature sensor array and the top surface of the pressure sensor array (that is, silicon rigid cavities) induced hydroxyl termination for bonding. After the alignment of the stacked arrays of electrodes and temperature sensors with the pressure sensor array, heating at 70 °C for 10 min yielded strong bonding and completed the fabrication.

Characterization of the electrode array. A digital potentiostat (Metrohm Autolab) with an Ag–AgCl reference electrode and a Pt counter electrode captured the impedance spectrum of the electrode in 0.1 M PBS at room temperature. An impedance analyser (Keysight, E4990A) recorded the impedance between two electrodes at room temperature and 37 °C with 0.1 M PBS, hydrogel (2 wt% agar, 98 wt% 0.1 M PBS) or non-perfused tissue (for example, chicken breast) as the medium. Impedance maps at a fixed frequency (for example, 1 kHz) were from Intan 1024ch recording controller.

Characterization of the temperature sensor array. A customized circuit enabled automated measurement of the resistance of each temperature sensor in the array at different temperatures (from 30 to 80 °C). Calibrated spatial maps of the TCR corresponded to the slopes of the $\Delta R/R$ versus temperature curves defined by linear least-squares fitting to the data. An infrared camera (FLIR A655sc) provided spatiotemporal temperature measurements at a sampling rate of 20 Hz for comparisons.

Characterization of the pressure sensor array. A customized circuit enabled automated measurement of the resistance of each pressure sensor in the array

at different pressures. Calibrated spatial maps of sensitivity corresponded to the slopes of the $\Delta R/R$ versus pressure curves defined by linear least-squares fitting to the data. A dynamic mechanical analysis system (DMA, TA Instruments RSA G2) provided a means for programmable and automatic loading–unloading and measurements of the force at a sampling rate of 30 Hz as the reference for pressure measurement.

Mechanical test. A customized mechanical stage enabled the application of precisely controlled biaxial strains to the electronics. A linear stage (Aerotech, ATS100-150) with a LabVIEW control interface provided capabilities for cyclic uniaxial stretching tests.

RFA. Sinusoidal voltages with amplitudes ranging from 10 to 40 V at a frequency of 400 kHz served as the signals for RFA. The temperature sensor array or an infrared microscope (Optotherm, Thermal imaging system) were used to record the temperature during RFA. In the case of measurement with an infrared microscope, the recorded values corresponded to the temperatures at the back surface of the electrode array (that is, the surface of the bottom PI layer). Media for in vitro RFA included 0.1 M PBS, hydrogel (2 wt% agar, 98 wt% 0.1 M PBS) and non-perfused tissues in 0.1 M PBS at room temperature and 37 °C.

IRE ablation. Biphasic pulses with amplitudes of ~200 V and durations of 100 μs served as the signals for IRE. Temperature measurements during IRE used an infrared microscope (Optotherm, Thermal imaging system). The recorded values were the temperatures at the back surface of the electrode array (that is, the surface of the bottom PI layer). In vitro IRE tests exploited potato models at room temperature.

Multiplexed data acquisition and signal processing. For electrogram mapping, anisotropic conductive film and laser-defined flexible printed circuit board (PCB) connectors connected the electrode array to a zero insertion force connector soldered to a customized PCB board. The PCB board connected to the Intan 1024ch recording controller through two 36-pin wire adapters, a 64-channel amplifier board (RHD2164), and a serial peripheral interface cable. A commercial software interface simultaneously recorded electrograms from 64 channels at a sampling rate of 20 kS s^{-1}. The bandwidth of the amplifier hardware extended from 0.1 to 200 Hz. A notch filter at 60 Hz further reduced the noise signal from electrical wires. For temperature and pressure mapping, an anisotropic conductive film cable and laser-defined flexible PCB connectors connected the arrays of temperature and pressure sensors to a customized PCB board. Wires from the PCB board joined the sensors to a customized circuit for time-division multiplexing. A PowerLab computer interface (ADInstruments, Model 8/35) recorded the signal from the common path at a sampling rate of 200 kS s^{-1}. A square wave at 5 kHz, generated from the PowerLab computer interface, served as the clock signal for multiplexing. Customized MATLAB code decoded the signal from one common path into 64 traces of signals that correspond with the 64 individual sensors. A digital moving-mean filter with a window size of 20 smoothed the 64 demultiplexed signals.

Synchronized recording. Synchronized measurements of temperatures from the temperature sensor array and the infrared camera relied on the absolute time recorded from both the PowerLab computer interface (ADInstruments, Model 8/35) and the infrared camera (FLIR A655sc). Synchronized measurements from the pressure sensor array and the commercial force gauge (DMA, TA Instruments RSA G2) used the absolute time recorded from the PowerLab computer interface and the created or modified time of the file from the gauge for alignment. Synchronized measurements of electrograms from the Intan recording controller and optical signals from the MiCAM05 exploited the MARK OUT port from the Intan system. The MARK OUT port sent a digital pulse to trigger the optical mapping. Synchronized measurements of pressures and electrograms were based on two PowerLab computer interfaces. One PowerLab computer interface recorded the ECG through commercial electrodes, provided electrical output to another commercial electrodes for pacing, and generated a trigger signal using the TRIGGER port at the start of the measurement. The other PowerLab computer interface measured the trigger signal as a marker for alignment, and provided clock and reset signals to control the customized circuit for pressure mapping. Synchronized measurements of temperatures from the temperature array during RFA used the PowerLab computer interface to provide clock and reset signals to control the customized circuit for temperature mapping. The radiofrequency signal generator sent a synchronized signal to the PowerLab computer interface as a marker at the starting point of RFA.

Finite element analysis. ABAQUS/Standard v2016 software was used for static finite element simulations of the mechanical deformations of the electrodes, temperature sensors and pressure sensors under multiple boundary and loading conditions—that is, in-plane and out-of-plane tension and compression and out-of-plane pressure. The finite element mesh of the electrodes, temperature sensors and pressure sensors comprised four-node rectangular elements and linear shape functions in plane stress with reduced integration (S4R). Eight-node solid element with linear shape functions and reduced integration (C3D8R) modelled

the underlying substrate. The elements had uniform size and each interconnect had at least six elements across its thickness. Enhanced hourglass control was used to ensure accuracy. Simulations of the silicone elastomers (Ecoflex and Dragon Skin) exploited the hyperelastic model following the Mooney–Rivlin law described by

$$U = C_{10}\left(\overline{I_1} - 3\right) + C_{01}\left(\overline{I_2} - 3\right) + \frac{1}{D_1}\left(J^{el} - 1\right)^2 \tag{2}$$

where U is the strain energy per unit of reference volume; C_{10}, C_{01} and D_1 are temperature-dependent material parameters; $\overline{I_1}$ and $\overline{I_2}$ are the first and second deviatoric strain invariants; and J^{el} is the elastic volume ratio. Simulations for PI and silicon used linear elastic material models ($E = 2.5$ GPa, $\nu = 0.34$ for PI, and $E = 112.4$ GPa, $\nu = 0.28$ for silicon). Modelling of Au was based on the ideal elastic–plastic model (Young's modulus $E = 79$ GPa, Poisson's ratio $\nu = 0.44$, yield strength = 237 MPa). The commercial software COMSOL (v.5.3) was adopted to predict the tissue ablation with coupled multifields of electric currents, bioheat transfer and electrical circuit. The electric currents module yielded the predictions of the electric field distribution in resistive heating. The bioheat transfer module yielded the predictions of the heat transfer and tissue ablation or injury. The electrical circuit module allowed the investigation of the potential drop on electrode due to the resistance of stretchable interconnections. In addition, the simulation of tissue ablation included latent heat of evaporation of water (2.4112×10^6 J kg^{-1}) as a domain source. The tissue damage with energy-absorption type was included in the bioheat transfer module. The material parameters (density ρ, thermal conductivity k, electric conductivity σ and heat capacity at constant pressure C_p) are shown in Supplementary Table 2.

Animal experiments. The experiments were conducted in accordance with the ethical guidelines of the National Institutes of Health and with the approval of the Institutional Animal Care and Use Committee of the George Washington University in Washington DC. Three adult female New Zealand white rabbits were used for the instrumented balloon catheter validation. This was a prospective and non-randomized study as there was only one group. Representative data from one of the experiments are presented here. The details of the whole-heart rabbit preparation have been previously described[39]. In brief, the heart was placed in a temperature-controlled bath at 37 °C and perfused under constant pressure (60 mmHg) with oxygenated Tyrode's solution. The heart was immobilized using 10 μM blebbistatin (Cayman Chemical) to eliminate motion artifacts and the voltage-sensitive dye di-4-ANBDQBS (Potentiometric Probes) was used to stain the tissue. After a stabilization period of 20–30 min, optical or electrical recordings were acquired.

Donor human heart experiments. The experiments using human heart tissue were approved by the Institutional Review Board (Office of Human Research) at the George Washington University. The two de-identified donor human hearts were procured from Washington Regional Transplant Community in Washington, DC. As with the animal experiments, this was a prospective, non-randomized study to validate the devices. The human left ventricle wedge preparations have been described previously[40]. In brief, wedges from the posterolateral left ventricle free wall perfused via the left marginal artery were dissected, cannulated and mounted in a tissue chamber. The tissue was perfused with Tyrode solution and treated with blebbistatin and the near-infrared fluorescent dye di-4-ANBDQBS to minimize motion artifacts and stain the tissue, respectively. The electrical and optical recordings were similarly acquired. The optical and electrical data were analysed using the custom MATLAB software RHYTHM and PFEIFER[41], respectively.

Reporting summary. Further information on research design is available in the Nature Research Reporting Summary linked to this article.

Data availability
The main data supporting the results in this study are available within the paper and its Supplementary Information. Source data for the figures are available from figshare with the identifier https://doi.org/10.6084/m9.figshare.12631835.

Code availability
The custom MATLAB software for data analysis can be downloaded from https://github.com/optocardiography.

References
1. Biere, S. S. et al. Minimally invasive versus open oesophagectomy for patients with oesophageal cancer: a multicentre, open-label, randomised controlled trial. *Lancet* **379**, 1887–1892 (2012).
2. Bacha, E. & Kalfa, D. Minimally invasive paediatric cardiac surgery. *Nat. Rev. Cardiol.* **11**, 24–34 (2014).

3. Martens, T. P. et al. Percutaneous cell delivery into the heart using hydrogels polymerizing in situ. *Cell Transplant.* **18**, 297–304 (2009).

4. Oxley, T. J. et al. Minimally invasive endovascular stent-electrode array for high-fidelity, chronic recordings of cortical neural activity. *Nat. Biotechnol.* **34**, 320–327 (2016).

5. Kim, D.-H. et al. Dissolvable films of silk fibroin for ultrathin conformal bio-integrated electronics. *Nat. Mater.* **9**, 511–517 (2010).

6. Dukkipati, S. R. et al. Visual balloon-guided point-by-point ablation: reliable, reproducible, and persistent pulmonary vein isolation. *Circ. Arrhythm. Electrophysiol.* **3**, 266–273 (2010).

7. Wazni, O., Wilkoff, B. & Saliba, W. Catheter ablation for atrial fibrillation. *N. Engl. J. Med.* **365**, 2296–2304 (2011).

8. Kim, D.-H. et al. Materials for multifunctional balloon catheters with capabilities in cardiac electrophysiological mapping and ablation therapy. *Nat. Mater.* **10**, 316–323 (2011).

9. Roche, E. T. et al. A light-reflecting balloon catheter for atraumatic tissue defect repair. *Sci. Transl. Med.* **7**, 306ra149 (2015).

10. Lee, S. P. et al. Catheter-based systems with integrated stretchable sensors and conductors in cardiac electrophysiology. *Proc. IEEE* **103**, 682–689 (2015).

11. Kim, Y., Parada, G. A., Liu, S. & Zhao, X. Ferromagnetic soft continuum robots. *Sci. Robot.* **4**, eaax7329 (2019).

12. Ashammakhi, N. et al. Minimally invasive and regenerative therapeutics. *Adv. Mater.* **31**, 1804041 (2019).

13. Fang, H. et al. Capacitively coupled arrays of multiplexed flexible silicon transistors for long-term cardiac electrophysiology. *Nat. Biomed. Eng.* **1**, 0038 (2017).

14. Hua, Q. et al. Skin-inspired highly stretchable and conformable matrix networks for multifunctional sensing. *Nat. Commun.* **9**, 244 (2018).

15. Chung, H. U. et al. Binodal, wireless epidermal electronic systems with in-sensor analytics for neonatal intensive care. *Science* **363**, eaau0780 (2019).

16. Sharma, T., Aroom, K., Naik, S., Gill, B. & Zhang, J. X. Flexible thin-film PVDF-TrFE based pressure sensor for smart catheter applications. *Ann. Biomed. Eng.* **41**, 744–751 (2013).

17. Klinker, L. et al. Balloon catheters with integrated stretchable electronics for electrical stimulation, ablation and blood flow monitoring. *Extrem. Mech. Lett.* **3**, 45–54 (2015).

18. Lee, K. et al. Microneedle drug eluting balloon for enhanced drug delivery to vascular tissue. *J. Control. Release* **321**, 174–183 (2020).

19. Liu, Z. et al. Transcatheter self-powered ultrasensitive endocardial pressure sensor. *Adv. Funct. Mater.* **29**, 1807560 (2019).

20. Bergmann, O. et al. Dynamics of cell generation and turnover in the human heart. *Cell* **161**, 1566–1575 (2015).

21. Xu, S. et al. Assembly of micro/nanomaterials into complex, three-dimensional architectures by compressive buckling. *Science* **347**, 154–159 (2015).

22. Wu, J.-F. Scanning approaches of 2-D resistive sensor arrays: a review. *IEEE Sens. J.* **17**, 914–925 (2016).

23. Gustafsson, S. E. Transient plane source techniques for thermal conductivity and thermal diffusivity measurements of solid materials. *Rev. Sci. Instrum.* **62**, 797–804 (1991).

24. Webb, R. C. et al. Ultrathin conformal devices for precise and continuous thermal characterization of human skin. *Nat. Mater.* **12**, 938–944 (2013).

25. Krishnan, S. R. et al. Epidermal electronics for noninvasive, wireless, quantitative assessment of ventricular shunt function in patients with hydrocephalus. *Sci. Transl. Med.* **10**, eaat8437 (2018).

26. Yokoyama, K. et al. Novel contact force sensor incorporated in irrigated radiofrequency ablation catheter predicts lesion size and incidence of steam pop and thrombus. *Circ. Arrhythm. Electrophysiol.* **1**, 354–362 (2008).

27. Ariyarathna, N., Kumar, S., Thomas, S. P., Stevenson, W. G. & Michaud, G. F. Role of contact force sensing in catheter ablation of cardiac arrhythmias: evolution or history repeating itself? *JACC Clin. Electrophysiol.* **4**, 707–723 (2018).

28. Yousef, H., Boukallel, M. & Althoefer, K. Tactile sensing for dexterous in-hand manipulation in robotics—a review. *Sens. Actuator A* **167**, 171–187 (2011).

29. Costa, P., Ribeiro, S. & Lanceros-Mendez, S. Mechanical vs. electrical hysteresis of carbon nanotube/styrene–butadiene–styrene composites and their influence in the electromechanical response. *Compos. Sci. Technol.* **109**, 1–5 (2015).

30. Jang, K.-I. et al. Self-assembled three dimensional network designs for soft electronics. *Nat. Commun.* **8**, 15894 (2017).

31. Dewire, J. & Calkins, H. State-of-the-art and emerging technologies for atrial fibrillation ablation. *Nat. Rev. Cardiol.* **7**, 129–138 (2010).

32. Maor, E. et al. Pulsed electric fields for cardiac ablation and beyond: A state-of-the-art review. *Heart Rhythm* **16**, 1112–1120 (2019).

33. Hjouj, M. & Rubinsky, B. Magnetic resonance imaging characteristics of nonthermal irreversible electroporation in vegetable tissue. *J. Membr. Biol.* **236**, 137–146 (2010).

34. Ramer, O. Integrated optic electrooptic modulator electrode analysis. *IEEE J. Quantum Electron.* **18**, 386–392 (1982).

35. Nath, S., DiMarco, J. P. & Haines, D. E. Basic aspects of radiofrequency catheter ablation. *J. Cardiovasc. Electrophysiol.* **5**, 863–876 (1994).

36. McClintock, R. Strain gauge calibration device for extreme temperatures. *Rev. Sci. Instrum.* **30**, 715–718 (1959).

37. Hur, S.-G., Kim, D.-J., Kang, B.-D. & Yoon, S.-G. Effect of the deposition temperature on temperature coefficient of resistance in CuNi thin film resistors. *J. Vac. Sci. Technol. B* **22**, 2698–2701 (2004).

38. Pikul, J. et al. Stretchable surfaces with programmable 3D texture morphing for synthetic camouflaging skins. *Science* **358**, 210–214 (2017).

39. Gloschat, C. et al. RHYTHM: an open source imaging toolkit for cardiac panoramic optical mapping. *Sci. Rep.* **8**, 2921 (2018).

40. Aras, K. K., Faye, N. R., Cathey, B. & Efimov, I. R. Critical volume of human myocardium necessary to maintain ventricular fibrillation. *Circ. Arrhythm. Electrophysiol.* **11**, e006692 (2018).

41. Rodenhauser, A. et al. PFEIFER: Preprocessing framework for electrograms intermittently fiducialized from experimental recordings. *J. Open Source Softw.* **3**, 472 (2018).

Acknowledgements

Author contributions

M.H., L.C., K.A., R.G., Y.H., I.R.E. and J.A.R. conceived the ideas, designed the experiments and wrote the manuscript; L.C., K.L. and G.Y. performed mechanical, electrical and thermal modelling. M.H., C. Liang, B.S., J.-H.K., Q.Y., Y.M., E.S., J.M.B., Y.L., C. Liu and J.B.M. fabricated the devices; M.H., X.C., H.Z., B.S., W.B., Y.M. and W.L. performed in vitro data collection and analysis; M.H., K.A., H.Z. and N.R.F. performed ex vivo data collection and analysis.

Competing interests

The authors declare no competing interests.

Additional information

Supplementary information is available for this paper at https://doi.org/10.1038/s41551-020-00604-w.

Correspondence and requests for materials should be addressed to Y.H., I.R.E. or J.A.R.

Peer review information Peer reviewer reports are available.

Reprints and permissions information is available at www.nature.com/reprints.

Publisher's note Springer Nature remains neutral with regard to jurisdictional claims in published maps and institutional affiliations.

nature research

Corresponding author(s):   Yonggang Huang, Igor R. Efimov and John A. Rogers

Last updated by author(s):   Jul 9, 2020

Reporting Summary

Nature Research wishes to improve the reproducibility of the work that we publish. This form provides structure for consistency and transparency in reporting. For further information on Nature Research policies, see Authors & Referees and the Editorial Policy Checklist.

Statistics

For all statistical analyses, confirm that the following items are present in the figure legend, table legend, main text, or Methods section.

n/a	Confirmed	
☐	☒	The exact sample size (n) for each experimental group/condition, given as a discrete number and unit of measurement
☐	☒	A statement on whether measurements were taken from distinct samples or whether the same sample was measured repeatedly
☐	☒	The statistical test(s) used AND whether they are one- or two-sided *Only common tests should be described solely by name; describe more complex techniques in the Methods section.*
☒	☐	A description of all covariates tested
☐	☒	A description of any assumptions or corrections, such as tests of normality and adjustment for multiple comparisons
☐	☒	A full description of the statistical parameters including central tendency (e.g. means) or other basic estimates (e.g. regression coefficient) AND variation (e.g. standard deviation) or associated estimates of uncertainty (e.g. confidence intervals)
☒	☐	For null hypothesis testing, the test statistic (e.g. F, t, r) with confidence intervals, effect sizes, degrees of freedom and P value noted *Give P values as exact values whenever suitable.*
☒	☐	For Bayesian analysis, information on the choice of priors and Markov chain Monte Carlo settings
☒	☐	For hierarchical and complex designs, identification of the appropriate level for tests and full reporting of outcomes
☐	☒	Estimates of effect sizes (e.g. Cohen's d, Pearson's r), indicating how they were calculated

Our web collection on statistics for biologists contains articles on many of the points above.

Software and code

Policy information about availability of computer code

Data collection	Multiplexed temperature and pressure sensing: Powerlab with Labchart 8 Electrogram and impedance mapping: Intan Instrument with RHS Stim/Recording Controller Force and pressure: custom Labview program, MESUR gauge Software, TA Instruments TRIOS, Thermal imaging: FLIR Tools+ software, Optotherm Micro Thermal Imaging System
Data analysis	Labchart 8, Matlab 2017a with custom code available at: http://intantech.com/downloads.html?tabSelect=Software, and https://github.com/optocardiography

For manuscripts utilizing custom algorithms or software that are central to the research but not yet described in published literature, software must be made available to editors/reviewers. We strongly encourage code deposition in a community repository (e.g. GitHub). See the Nature Research guidelines for submitting code & software for further information.

Data

Policy information about availability of data

All manuscripts must include a data availability statement. This statement should provide the following information, where applicable:

- Accession codes, unique identifiers, or web links for publicly available datasets
- A list of figures that have associated raw data
- A description of any restrictions on data availability

The main data supporting the results in this study are available within the paper and its Supplementary Information. Source data for the figures are available from figshare with the identifier https://doi.org/10.6084/m9.figshare.12631835 (ref. 42).

Field-specific reporting

Please select the one below that is the best fit for your research. If you are not sure, read the appropriate sections before making your selection.

☒ Life sciences   ☐ Behavioural & social sciences   ☐ Ecological, evolutionary & environmental sciences

For a reference copy of the document with all sections, see nature.com/documents/nr-reporting-summary-flat.pdf

Life sciences study design

All studies must disclose on these points even when the disclosure is negative.

Sample size	n = 1. Ex vivo experiments require only 1 successful demonstration because of their proof-of-concept nature.
Data exclusions	No data were excluded from the analyses.
Replication	Experiments were replicated multiple times.
Randomization	Randomization was not required.
Blinding	The personnel completing the data analyses were blinded to the experimental groups.

Reporting for specific materials, systems and methods

We require information from authors about some types of materials, experimental systems and methods used in many studies. Here, indicate whether each material, system or method listed is relevant to your study. If you are not sure if a list item applies to your research, read the appropriate section before selecting a response.

Materials & experimental systems

n/a	Involved in the study
☒	☐ Antibodies
☒	☐ Eukaryotic cell lines
☒	☐ Palaeontology
☐	☒ Animals and other organisms
☐	☒ Human research participants
☒	☐ Clinical data

Methods

n/a	Involved in the study
☒	☐ ChIP-seq
☒	☐ Flow cytometry
☒	☐ MRI-based neuroimaging

Animals and other organisms

Policy information about studies involving animals; ARRIVE guidelines recommended for reporting animal research

Laboratory animals	Adult female New Zealand white rabbits.
Wild animals	The study did not involve wild animals
Field-collected samples	The study did not involve samples collected from the field
Ethics oversight	The experiments were conducted in accordance with the ethical guidelines of the National Institutes of Health and with the approval of the Institutional Animal Care and Use Committee of the George Washington University in Washington DC.

Note that full information on the approval of the study protocol must also be provided in the manuscript.

Human research participants

Policy information about studies involving human research participants

Population characteristics	The two de-identified donor human hearts were procured from Washington Regional Transplant Community in Washington, DC.
Recruitment	This was a prospective, non-randomized study to validate the devices.
Ethics oversight	The experiments using human heart tissue were approved by the Institutional Review Board (Office of Human Research) at the George Washington University.

Note that full information on the approval of the study protocol must also be provided in the manuscript.